OPTICS

Multi-watt, multi-octave, mid-infrared femtosecond source

Marcus Seidel,[1]*† Xiao Xiao,[1] Syed A. Hussain,[2] Gunnar Arisholm,[3] Alexander Hartung,[4] Kevin T. Zawilski,[5] Peter G. Schunemann,[5] Florian Habel,[2] Michael Trubetskov,[1] Vladimir Pervak,[2] Oleg Pronin,[1]† Ferenc Krausz[1,2]

Spectroscopy in the wavelength range from 2 to 11 μm (900 to 5000 cm^{-1}) implies a multitude of applications in fundamental physics, chemistry, as well as environmental and life sciences. The related vibrational transitions, which all infrared-active small molecules, the most common functional groups, as well as biomolecules like proteins, lipids, nucleic acids, and carbohydrates exhibit, reveal information about molecular structure and composition. However, light sources and detectors in the mid-infrared have been inferior to those in the visible or near-infrared, in terms of power, bandwidth, and sensitivity, severely limiting the performance of infrared experimental techniques. This article demonstrates the generation of femtosecond radiation with up to 5 W at 4.1 μm and 1.3 W at 8.5 μm, corresponding to an order-of-magnitude average power increase for ultrafast light sources operating at wavelengths longer than 5 μm. The presented concept is based on power-scalable near-infrared lasers emitting at a wavelength near 1 μm, which pump optical parametric amplifiers. In addition, both wavelength tunability and supercontinuum generation are reported, resulting in spectral coverage from 1.6 to 10.2 μm with power densities exceeding state-of-the-art synchrotron sources over the entire range. The flexible frequency conversion scheme is highly attractive for both up-conversion and frequency comb spectroscopy, as well as for a variety of time-domain applications.

INTRODUCTION

The generation of broadband, intense femtosecond light pulses has enabled the observation and manipulation of molecular motions (*1*), as well as triggering extreme nonlinear effects such as high-order harmonic generation (*2*) or petahertz current switching in solids (*3*). The sources of femtosecond pulses, mode-locked oscillators, can also provide well-controlled frequency combs, which have revolutionized precision spectroscopy in a multitude of disciplines ranging from atomic physics to astrophysics (*4*). These examples manifest that femtosecond lasers constitute an extremely versatile tool for a vast variety of time- and frequency-domain applications—a tool that is, however, most advanced in the near-infrared (NIR) and the visible. The most powerful femtosecond sources operate around 1-μm wavelength. Up to kilowatt average powers have been obtained from laser amplifiers (*5*). With longer wavelengths, the power levels strongly decrease. For example, broadband gain that allows femtosecond operation has only been demonstrated up to 2.9 μm with approximately 300 mW of average power (*6*).

An alternative route to femtosecond pulse generation in the mid-infrared (MIR) exploits quadratic [$\chi^{(2)}$-type] nonlinear optical effects, namely, difference frequency generation of two NIR beams (*7*, *8*). Multiple watt-level megahertz-rate femtosecond sources have been demonstrated in the wavelength range between 3 and 4 μm (*9*–*11*), partially with carrier-envelope phase stabilization (*12*), which is crucial for several time-domain applications, for example, electro-optical sampling (*13*), as well as for frequency comb spectroscopy (*14*). The reported average powers from femtosecond sources with wavelengths longer than 5 μm are significantly lower than those from shorter-wavelength sources (*14*). This is caused by multi-phonon absorptions of all nonlinear crystals containing oxides. In general, it is extremely difficult to pump non-oxide crystals with 1-μm femtosecond sources, as Petrov (*7*) points out. Just recently, 100-milliwatt average power levels have been reached with several down-conversion approaches (*11*, *15*), among them one with passive carrier-envelope phase stabilization (*13*).

The lack of a variety of powerful femtosecond MIR sources stands in strong contrast to the multitude of applications in the spectral region. Because vibrational transitions arise from molecular structure, MIR radiation is used in a variety of chemical analysis techniques (*16*), for example, in trace gas and human breath analysis (*17*) as well as early cancer detection (*18*). Particularly interesting experimental techniques are frequency comb (*14*), up-conversion, (*19*) and two-dimensional infrared spectroscopy (*20*). All these techniques rely on or at least strongly benefit from femtosecond pulses. In addition, the temporal compression of broadband MIR pulses to a few optical cycles has revealed strong-field effects, such as high-harmonic generation from atomic gases well into the x-ray regime (*21*) or the occurrence of Bloch oscillations in semiconductors (*22*). In these examples, high peak power is required for accessing the regime of extreme nonlinear optics. On the other hand, high average power and photon flux result in light source brightness surpassing those available from synchrotron sources (*13*) and consequently facilitate the use of (rather noisy) uncooled MIR detectors or detector arrays (*23*). Moreover, high average power is important for experimental techniques with low yield such as stand-off gas detection (*24*) and may avoid the need for multiple interactions with the sample in resonant cavities or multipass cells (*17*).

Here, the issue of the scarce availability of high-power femtosecond sources in the MIR is addressed by taking advantage of the most powerful laser architectures in the NIR and frequency down-converting their radiation by means of optical parametric amplification. The generation of about 5 W of average power at 4 μm and more than 1 W of

[1]Max-Planck-Institut für Quantenoptik, Hans-Kopfermann-Str. 1, D-85748 Garching, Germany. [2]Ludwig-Maximilians-Universität München, Am Coulombwall 1, D-85748 Garching, Germany. [3]FFI (Norwegian Defence Research Establishment), P.O. Box 25, NO-2027 Kjeller, Norway. [4]Leibniz-Institute of Photonic Technology, Albert-Einstein-Straße 9, D-07745 Jena, Germany. [5]BAE Systems, P.O. Box 868, Nashua, NH 03063, USA.
*Present address: Institut de Science et d'Ingénierie Supramoléculaires, 8 allée Gaspard Monge, 67000 Strasbourg, France.
†Corresponding author. Email: marcus.seidel@mpq.mpg.de (M.S.); oleg.pronin@mpq.mpg.de (O.P.)

average power at 8.5 μm is demonstrated. In addition, using the 4-μm source yielded a supercontinuum with two-octave spectral coverage from 1.6 to 7.1 μm at unprecedented high-power spectral densities.

RESULTS

Optical parametric amplifiers

Optical parametric amplifiers (OPAs) have been used as frequency down-converters. Two versions of the setup shown in Fig. 1 were implemented. The first used a periodically poled MgO:$LiNbO_3$ (PPLN) nonlinear crystal and was seeded with the continuum emerging from a 20-cm-long polarization-maintaining all-normal dispersion fiber with a mode field diameter of 2.7 μm. The second version, for longer MIR wavelengths, used a $LiGaS_2$ (LGS) nonlinear crystal and was seeded with the continuum emerging from a large mode area fiber with a mode field diameter of 10.3 μm, exhibiting also normal dispersion (see Materials and Methods).

In both OPAs, the output of a Kerr-lens mode-locked thin-disc oscillator (*25*) directly served as the pump source for the down-conversion process. The thin-disc oscillator operated at 50 W of average power and a central wavelength of 1.03 μm. It emitted 1.3-μJ, 230-fs pulses at a repetition rate of 37.5 MHz. In the OPA setup, the long-wavelength parts of the fiber continua, which are shown in Fig. 2, were collinearly and temporally overlapped with the pump radiation by means of a dichroic mirror. Seed and pump radiation were sent into the nonlinear crystal, where their MIR difference frequency was generated. The setup avoids spatial chirp of the MIR and results in passive stabilization of its carrier-envelope phase (*26*).

For generating radiation with wavelengths up to 5 μm, oxide crystals can be used. Here, a 5-mm-long PPLN crystal with a 1 × 1 mm^2 aperture per poling period was used. Its wide transparency range (0.32 to 5.5 μm), high figure of merit of about 24 pm^2/V^2 (*27*), and temporal walk-off suppression by parametric gain guiding (*28*) enabled efficient amplification. Crystal length and focus size have been optimized for maximizing the infrared output (see Materials and Methods). Figure 3 shows a comparison of MIR power predicted from simulations and extracted from experiments. A poling period of 28 μm was used, resulting in a wavelength of 4.1 μm. With a tight focusing geometry ($1/e^2$ diameter, d = 120 μm), about 75% of the pump photons could be down-converted, corresponding to a MIR average power of 0.9 W. This might be an attractive scheme for commercially available oscillators (*11*, *15*). Upon extracting the full 42-W pump power of the thin-disc oscillator, a maximal MIR power of 5.1 W was generated. The spot diameter had to be increased to 300 μm in this case. The OPA still down-converted about 50% of the incident pump photons.

For wavelengths longer than 5 μm, an LGS crystal was used. LGS is transparent in the range between 0.33 and 11.6 μm (*29*), and its dispersion allows broadband amplification of the seed when pumped at 1.03 μm (see section S5). With this highly favorable properties, the crystal presents an important exception among other non-oxide nonlinear crystals (*7*). Unfortunately, at present, the available LGS quality is, from our experience, still inferior to that of PPLN. Section S5 comments explicitly on the issue of crystal damage. To the best of the authors' knowledge, the first femtosecond OPA that uses this crystal in combination with 1-μm pump radiation is reported here. Both type I (seed and MIR have the same polarization) and type II (seed and MIR have orthogonal polarization) phase-matched crystals were studied. Figure 3 shows that up to 1.3 W of MIR at 8.5 μm was generated from a 7-mm-long, type II phase-matched crystal with an aperture of 3 x 3 mm^2 and specified cut angles of θ = 90° and ϕ = 38.8°. Because the figure of merit of LGS (~3.9 pm^2/V^2 for type II and ~ 2.3 pm^2/V^2 for type I phase matching) is lower than for PPLN, the OPA was seeded with increased spectral power (Fig. 2) and only up to 30 W could be used for pumping. A spot size of 230 μm was chosen. About 35% of the pump photons were down-converted.

Tunability

Tunability of the OPAs was investigated in the next step. The results are shown in Fig. 4. The poling periods of the PPLN crystal ranged from 25.5 to 28 μm. Consequently, the MIR radiation was tunable from about 4 to 5 μm. For all periods, more than 2 W of average power was generated. For longer wavelengths, the LGS OPA was used. It was operated

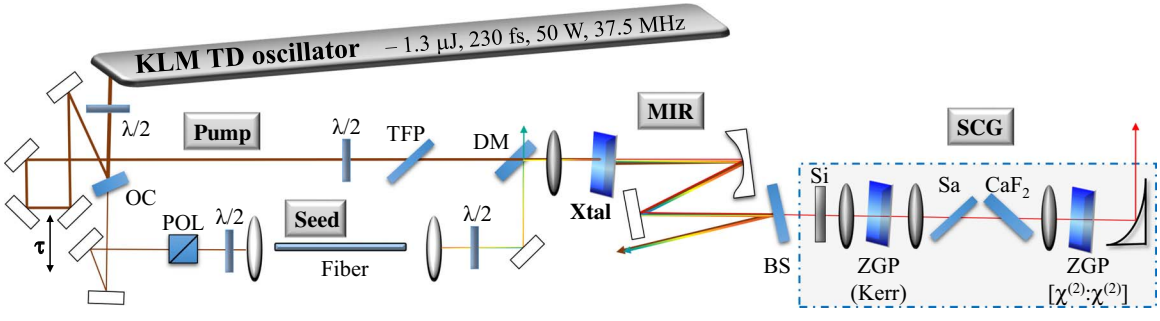

Fig. 1. OPA setup. The Kerr-lens mode-locked Yb:YAG thin-disc oscillator delivers 1.3-μJ pulses of 230-fs duration with a 37.5-MHz repetition rate. A dielectric mirror (OC) transmits either 3% or 15% of the oscillator power. The reflected light can be attenuated by a half-wave plate (λ/2) and thin-film polarizer (TFP) sequence and is directly used to pump the nonlinear crystal (Xtal), which is either PPLN or LGS. The seed generation is accomplished in a fiber with either a 2.7-μm (for PPLN) or 10.3-μm (for LGS) mode-field diameter. To suppress cross-phase modulation, the polarization is cleaned in front of the fiber. Aspheric lenses were used for coupling and collimation. The long wavelengths of the continuum and the pump are overlapped in space with a dichroic mirror (DM) and in time with a translation stage in the pump arm (τ). The polarizations of seed and pump are optimized for maximal conversion to the MIR. After the nonlinear crystal, the beams are collimated. The MIR is separated by means of a beam splitter (BS). The optics in the box with the dashed blue outline were only set up for supercontinuum generation (SCG) after the PPLN OPA. All lenses in the box and the Si plate for dispersion compensation were made from silicon and anti-reflection–coated from 3 to 5 μm. The lenses were plano-convex. The first has a focal length of 75 mm, and the second and third have focal lengths of 25 mm. The supercontinuum was roughly collimated with a parabolic mirror of 2-inch focal length. The ZGP crystals are described in detail in the main text. For dispersion compensation after the first ZGP crystal, a 2-mm sapphire (Sa) and a 5-mm CaF_2 plate were inserted at Brewster's angle.

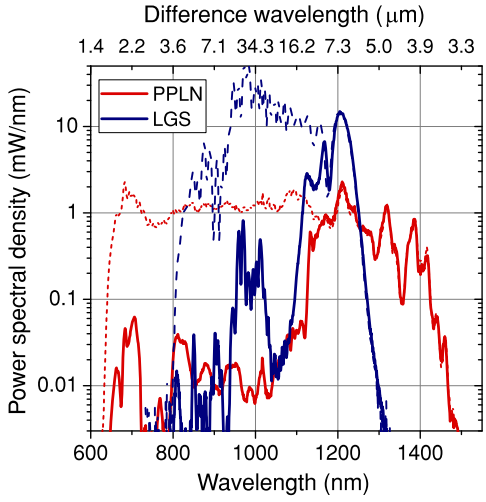

Fig. 2. Seed spectra. The dashed lines show the full fiber continua, and the solid lines show the seed spectra after the dichroic mirrors. The seed for the PPLN OPA is generated in a 20-cm polarization-maintaining fiber with normal dispersion and a 2.7-μm mode-field diameter (red lines). It theoretically allows the amplification of MIR wavelengths down to 3.3 μm. For amplifying wavelengths longer than 6 μm, it is beneficial to use the continuum generated in an 8-cm-long fiber with a 10.3-μm mode-field diameter (blue lines), which provides up to an order of magnitude more seed power. The filtered powers (solid lines) are 220 mW (PPLN OPA) and 800 mW (LGS OPA), respectively. The spectra are measured with an optical spectrum analyzer. The difference wavelength (λ_i) on the top axis refers to the central pump wavelength (λ_p = 1030 nm) and the seed wavelength on the bottom axis (λ_s), that is, $\lambda_i^{-1} = |\lambda_p^{-1} - \lambda_s^{-1}|$.

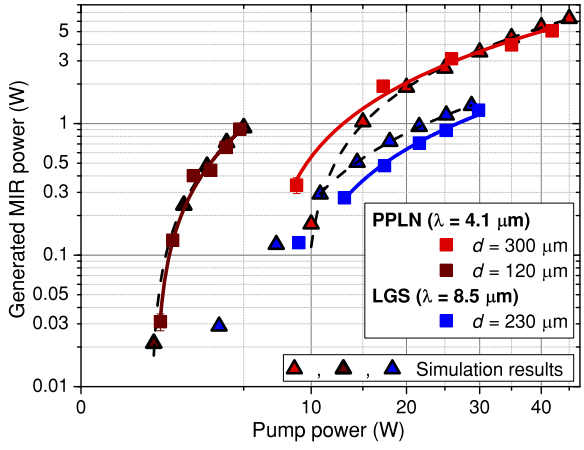

Fig. 3. MIR power. Simulation and experimental results for PPLN with a 28-μm poling period and LGS with a tuning angle of about ϕ = 38.6° (type II phase matching). For tight focusing into the PPLN (spot diameter *d* of the pump is 120 μm, wine red squares), up to 0.9 W of MIR was generated, which is in excellent agreement with the simulation (triangles with wine color filling; slope efficiency, 23%). If the full pump power was used (*d* = 300 μm, red squares), then 5.1 W of MIR at 4.1-μm wavelength was generated. The agreement with the simulations (triangles with red color filling) is good, although they predict a slightly steeper slope (slope efficiencies, 15 and 17.5%). For LGS (blue squares), a maximal power of 1.3 W was reached. This is also in good agreement with simulations (triangles with blue color filling; slope efficiencies, 5.4 and 6.0%). The *x* axis is scaled by the square root of the pump power, whereas the *y* axis is logarithmic, which represents the characteristic power relation for OPAs in the low depletion regime (*8*). The displayed lines show linear fits for extracting the slope efficiencies. All experimental results have been corrected for reflection losses.

most powerfully in the wavelength range from 7 to 9.5 μm. The MIR bandwidth in this spectral region is remarkable. Fourier transform limits of only two optical cycles were reached with a type I phase matching (vine red line, Fig. 4) despite using relatively long crystals. This stems from the favorable dispersion of LGS, which allows phase matching of two MIR frequencies at a single tuning angle (see section S5).

Supercontinuum generation

Supercontinuum generation makes the presented source attractive for molecular fingerprinting and time-domain applications requiring few-cycle pulses. For this purpose, cascaded quadratic nonlinearities were exploited. For the chalcopyrite $ZnGeP_2$ (ZGP) (*30*), an effective nonlinear refractive index of about -1×10^{-12} cm^2/W at a wavelength of 4.1 μm and tuning angle θ = 55° is estimated (see section S4). For comparison, the nonlinear refractive index of the used silica fibers is about 3×10^{-16} cm^2/W at the pump wavelength, that is, more than three orders of magnitude lower than near-phase–matched cascaded quadratic nonlinearity in ZGP.

The experimental setup of the continuum generation stage is shown in Fig. 1. In the first step, the pulses from the PPLN OPA were spectrally broadened in a 3-mm-thick ZGP crystal. At this stage, second-harmonic generation was avoided, and the nonlinearity mainly resulted from the optical Kerr effect. Consequently, the duration of the MIR pulses was reduced from 140 to 67 fs by means of material dispersion from sapphire and CaF_2 windows (see section S3). The compressed pulses were afterward focused into a 2-mm-thick ZGP crystal cut at θ = 55°, yielding the broadband radiation that is shown in Fig. 5. Including the generated second harmonic, the emerging spectrum spans from 1.6 to 7.1 μm (at −30 dB), which corresponds to more than two octaves. Simulations revealing more details about the continuum generation are presented in section S4. If combined with the broadband MIR radiation of the LGS OPA, about 2.7 octaves are covered, with a power spectral density exceeding microwatts per inverse centimeter over the whole range (Fig. 5).

DISCUSSION

The presented PPLN OPA unifies different advantages of the high-power frequency down-converters cited in the Introduction. The OPA emits multiple watts of average power with only 140-fs duration, avoids the need for active carrier-envelope phase stabilization, exhibits good power stability (see section S1), and consists of a simple setup. Although not further discussed within this context, if a pulse picker is added, then the system also presents an attractive source for two-photon microscopy in biomedical deep tissue imaging (*31*) because of the amplification of the seed around 1.3 μm.

Whereas PPLN and periodically poled $LiTaO_3$ are well-established crystals, which were used in previous studies (*9*–*12*, *26*), there are basically no commonly used non-oxide crystals, which are pumped with femtosecond NIR sources. Using a power-scalable laser architecture at a standard wavelength around 1 μm for pumping an OPA with an LGS crystal presents a novel concept for scalable long-wavelength infrared generation. It led to an immediate order-of-magnitude power increase for femtosecond sources in this spectral region. Moreover, the spectral bandwidth of the MIR was remarkably broad. A comparison to the results of Pupeza *et al.* (*13*) is instructive, where a 100-W mode-locked thin-disc oscillator was used for intrapulse difference frequency generation in a short LGS crystal. The OPA approach reported

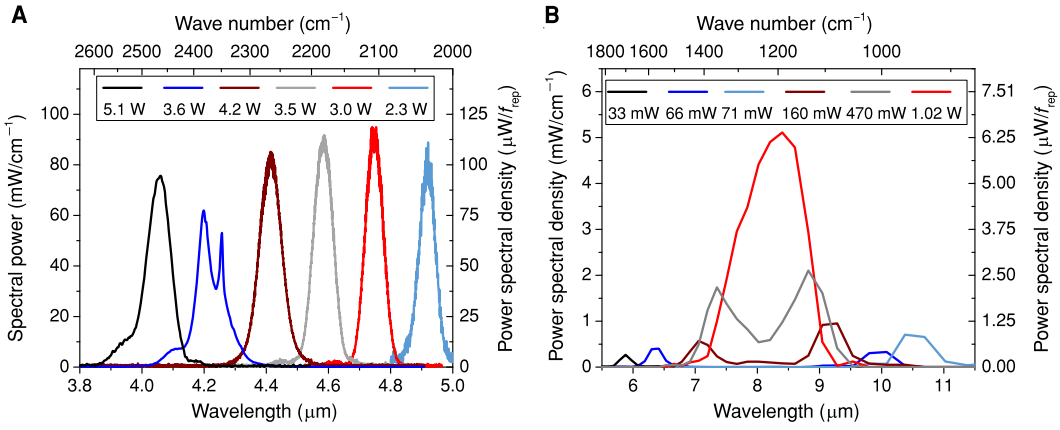

Fig. 4. Tuning curves. (**A**) Generated MIR power for maximal pump power and tuning periods from 28 to 25.5 μm (from left to right in −0.5-μm steps) of the PPLN. The spectrum centered at 4.2 μm is shaped through CO_2 absorption. The power was measured 25 cm behind the nonlinear crystal. (**B**) Tuning curve measured with a type I phase-matched LGS crystal. The OPA operates most powerfully around 8.2 μm (slightly blue-shifted from type II). Upon detuning from this central point, the phase-matched wavelengths split, allowing the generation of very broadband spectra (vine red line). The spectra below 6 μm (black line) and above 10 μm (light blue line) needed different delays to be generated because of the uncompressed seed pulse. With type I phase matching, a maximal MIR power of 1.0 W could be generated. Type I, however, allows the generation of slightly more broadband spectra than type II. More information is provided in section S5. Power spectral density is provided in units of mW/cm^{-1} and μW/f_{rep}, where f_{rep} = 37.5 MHz is the oscillator repetition rate. This unit is particularly interesting for frequency comb applications (*14*).

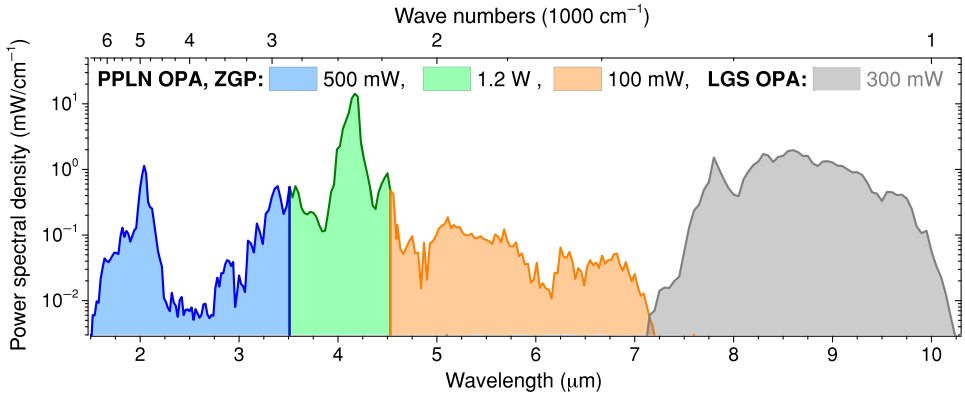

Fig. 5. Coverage of the MIR spectral region from 1.6 to 10.2 μm through two OPA channels. The supercontinuum spanning from 1.6 to 7.1 μm (at −30 dB) was generated in a 2-mm-thick ZGP crystal by means of cascaded quadratic nonlinearities. The continuum generation stage was pumped by 67-fs pulses emerging from the PPLN OPA and a precompression stage. The spectrum was recorded about 1.5 m away from the nonlinear crystal and partly shows strong attenuation due to atmospheric absorptions. The total average power of 1.8 W was measured behind the parabolic collimation mirror. A short-pass filter (blue area) and a long-pass filter (orange area) were used to determine the powers of the individual components. The gray area additionally shows the spectrum generated from a separate LGS OPA with a measured output power of 300 mW. Whereas both OPA channels could not be operated in parallel with the used pump laser, they can be readily combined at the presented power levels if a state-of-the-art mode-locked thin-disc oscillator (*34*) is used.

here led to 13-, 25-, and 35-fold increases in average power, conversion efficiency, and pulse energy, respectively. Despite the seven times longer crystal used in the OPA setup, the MIR Fourier transform limit, on the other hand, only increased by a factor of less than 2. This makes the approach also highly attractive for demanding applications in strong-field physics and extreme nonlinear optics, such as high-harmonic generation in gases (*21*).

The tuning curve of Fig. 4 covers a wide range of the MIR spectrum. The highest spectral power densities are achieved in the atmospheric transmission windows from 3 to 5 μm and 8 to 13 μm, which are particularly important for trace gas analysis (*14*). The high average powers are especially useful for stand-off detection (*24*). Using frequency comb spectroscopy for this purpose would require to lock a multiple of the laser repetition rate to a precise frequency reference or to use a second femtosecond laser for dual-comb spectroscopy (*14*, *17*). To extend the tuning range further, double-stage amplification schemes should be used (*11*). The presented scheme is limited by the seed bandwidth (supporting wavelengths down to about 3.3 μm; see Fig. 2) in short-wavelength MIR and by the LGS transparency (see section S5) in long-wavelength MIR.

The energy of the pulses with 4.1-μm central wavelength, after separating them from the amplified seed and the pump of the OPA, is about 90 nJ. This yields a combination of peak and average power, which is difficult to use in previously demonstrated supercontinuum generation schemes that extend to wavelengths beyond 5 μm. Exploiting the huge quadratic nonlinearities of ZGP presents an excellent alternative to the usage of chalcogenide waveguides (*32*) or filaments (*33*). This is substantiated in section S4. Despite reaching the spectral coverage from 1.6 to 10.2 μm only at −30 dB, the continuum still presents a significant advance in power spectral density. It may, for instance,

be compared to the continuum generated in chalcogenide fiber by Peterson *et al.* (*32*). They attained a spectral width (3 octaves) at −20 dB level, but only at a total average power of less than 1 mW. Consequently, the spectrum displayed in Fig. 5 presents more than two orders of magnitude increase in power spectral density.

The full 2.7 octaves were generated in two OPA channels. State-of-the-art mode-locked thin-disc oscillators (*34*) readily allow combining the output of LGS and PPLN OPA, and hence obtaining access to the whole MIR range in a single setup. A quasi-third channel results from type I second-harmonic generation in the ZGP crystal. Its spectrum covers the range from 1.6 to 2.5 μm and is orthogonally polarized with respect to the fundamental. For many spectroscopic applications, polarization is not of particular importance. For nonlinear methods, however, this has to be taken into account. The multiple channels of the supercontinuum suggest waveform synthesis, which has been recently demonstrated in the MIR with a kilohertz source (*35*). Studies on petahertz electronics (*3*) could be significantly extended by compressed pulses first because of the long driving wavelength and the associated impact on the electron trajectories in the electronic devices (*22*). Second, the megahertz repetition rate of the presented system would give insights into the reversibility of the current switching effects.

Upon attenuation of the most powerful parts of the spectrum shown in Fig. 5, the source would also become highly interesting for spectroscopy applications in biological matter, where watt average power levels would unnecessarily heat the samples. However, the demonstrated power spectral densities on the order of microwatts per inverse centimeter are typical for synchrotron radiation (*36*). Hence, the demonstrated laser-based source presents a compact alternative to the large-scale facilities that have found numerous applications in life sciences (*36*).

In conclusion, a highly powerful tool for advancing femtosecond MIR spectroscopy has been presented. Multiple watts of average power were generated between 4 and 5 μm, and for the first time, a watt-class femtosecond source operating beyond the multi-phonon absorption edge of oxide crystals was demonstrated. Likewise, the ultrashort pulses may give access to extreme nonlinear optical effects in solids and allow the study of ultrafast molecular dynamics. Furthermore, supercontinuum generation based on near-phase–matched cascaded quadratic nonlinearities resulted in significant spectral broadening toward longer wavelengths and would result in the coverage of the wavelength range from 1.6 to 10.2 μm (at −30 dB) with more than 2 W of total average power after combination of both OPA channels. This offers exciting opportunities for molecular fingerprinting, in particular with frequency up-conversion and field-sensitive techniques.

MATERIALS AND METHODS

Choice of crystals and spot size

The crystals MgO:$LiNbO_3$ and LGS exhibit bandgaps of about 4 eV, which is more than three times higher than the photon energy at 1030-nm vacuum wavelength. Consequently, no sign of detrimental multiphoton absorption was apparent even at maximal pump powers of 42 and 30 W, respectively. Both nonlinear crystals were fixed in a temperature-controlled copper mount, which was heated to about 60°C to avoid photorefractive effects and green-induced infrared absorption in PPLN.

The damage threshold of MgO:$LiNbO_3$ was initially tested with a 0.5-mm-thin sample and tight focusing. It was determined to be about 50 GW/cm^2. Under consideration of this limit, simulations were performed to determine the optimal spot size (see section S2). For LGS and the 230-fs pump pulses, a critical irradiance of 50 GW/cm^2 was assumed. This is in correspondence to the bandgap comparable to $LiNbO_3$ but rather conservative in comparison to the 1 TW/cm^2 threshold stated by Pupeza *et al.* (*13*) for 20-fs pulses.

However, in experiments with tight focusing and low average powers, damage of a thick crystal's end facet at much lower peak irradiances was noticed. This was attributed to self-focusing. Therefore, simulations were performed to reproduce the experimental observations. The nonlinear refractive index n_2 was varied until the pump beam collapsed at the end facet of the crystal, resulting in an estimate of $n_2 = 35 \times 10^{-16}$ cm^2/W, being about twice as large as the n_2 of $LiNbO_3$ (*37*). Unfortunately, because of the fact that LGS is still rather scarcely used, the available crystal quality is, from our experience, inferior to that of PPLN. Section S5 comments more explicitly on this issue. The reader is also referred to the methods section of Pupeza *et al.* (*13*).

For setting up the OPAs, simulations under the presence of pump and seed were conducted to determine the optimal spot sizes. In the experiment, these were measured with a pyroelectric rotating slit scanner. The temporal and spatial overlap was optimized at minimal pump power by means of parasitic sum frequency generation in PPLN. For LGS, a flip mirror behind the focusing lens was used to optimize the overlap of pump and seed by means of the sum frequency generation from a BBO crystal.

Choice of seed source

Normally dispersive photonic crystal fibers were chosen because they efficiently broaden the coupled pulses fairly symmetrically to longer and shorter wavelengths and typically exhibit good coherence properties. For the PPLN OPA, the use of the NL-1050-PM-NEG fiber (NKT Photonics) was necessary to reach sufficient seed bandwidth. It has a mode-field diameter of only 2.7 μm and a dispersion that is all-normal across the continuum region with a minimum group velocity dispersion of only about 2 fs^2/mm at 1050 nm. Therefore, the spectral parts resulting from optical wave breaking could be amplified. The polarization-maintaining version of the fiber was selected to maintain the coherence of the continuum despite the large broadening factors (see section S1) (*38*). For the long-wavelength OPA, sufficient bandwidth was provided by an 8-cm ESM12 fiber (NKT Photonics) with a 10.3-μm mode-field diameter. For this fiber length, self-phase modulation was saturated, whereas optical wave breaking beyond the zero-dispersion wavelength was avoided.

Power measurements

Power measurements were performed with thermal detectors. For the PPLN measurements, the Fresnel reflection of the rear surface of the uncoated crystal and the transmission of the single-sided coated beam splitter and of the silver mirrors were taken into account to calculate the values shown in Figs. 3 and 4. Moreover, a germanium plate was put in front of the power meter to block residual NIR. The transmission of this plate was assumed to be 46%, corresponding to an infinite number of Fresnel reflections.

The beam splitting after the LGS OPA was rather complicated because of the large energy difference between MIR and pump photons and the high average power. Using only a germanium plate led to a saturation of measured MIR power for pump powers higher than 10 W because of free carrier generation in the highly nonlinear semiconductor. Therefore, the total power incident on the germanium plate was reduced by directing only the front reflection of an uncoated ZnSe wedge onto it.

To additionally rule out contributions to the power measurement by heat generation in the germanium plate, seed and pump were delayed such that no MIR was generated anymore and a background measurement was taken. To cross-check whether the MIR power was determined correctly by this method, two alternative approaches were used. First, the total power of NIR and MIR was measured behind the OPA. Afterward, a 5-mm-thick glass plate was inserted, which only transmitted the NIR, that is, the difference of both measurements resulted in the MIR power. Second, a D-shaped mirror was used to reflect the NIR completely while the stronger diverging MIR was partly transmitted. All three methods were in good agreement with each other, confirming watt-level MIR generation. Recently, dielectric beam splitters with wide bandgap layer materials were coated in-house to separate MIR and NIR more efficiently.

Spectrum measurements

The seed spectra (Fig. 2) were measured with an optical spectrum analyzer. The spectra of Fig. 4 were measured with Fourier transform infrared (FTIR) spectrometers. The Bristol 721 spectrum analyzer was used for wavelengths up to 5 μm (Fig. 4A), and the Lasnix L-FTS was used for the LGS OPA measurements (Fig. 4B). Because of the inefficient beam splitting for the LGS OPA, all of the separated MIR power was sent to the FTIR. At the maximum of the tuning curve, the 1.0 W of average power was explicitly determined from a power meter measurement. The other average powers of Fig. 4B were derived from the area under the curves. To increase the signal-to-noise ratio, a monochromator (Newport/Oriel Cornerstone 260) was used for the continuum measurements of Fig. 5.

Supercontinuum generation

For the pulse compression stage, 5-mm silicon, 2- and 5-mm GaAs, 5-mm germanium, and 2- and 3-mm-thick ZGP plates were tested to achieve the strongest spectral broadening. Furthermore, the focal spot diameter was varied between 30 and 80 μm. The 3-mm-thick antireflection–coated ZGP crystal at a 80-μm spot diameter performed best and allowed compression of the MIR pulses to 67 fs after dispersion compensation by a 2-mm-thick sapphire plate (GVD ≈ −1700 fs^2/mm) and a 5-mm-thick CaF_2 plate (GVD ≈ −300 fs^2/mm). The pulses were measured via cross-correlation frequency-resolved optical gating (X-FROG; see section S3). For the supercontinuum generation, the nonlinear crystals were mounted such that they could be rotated around the propagation direction axis, tilted in the horizontal direction, and translated along the propagation direction. All free parameters were successively optimized under observation of the MIR spectrum. The broadest spectrum was achieved when the 2-mm-thick ZGP crystal, cut at θ = 55°, was positioned in the focus and was rotated to near-normal incidence. ZGP crystals of different thicknesses were not available for the experiments. The focal spot size of the supercontinuum stage was also about 80 μm. The spot sizes were measured with the pyroelectric rotating slit scanner.

Simulations

All simulations were performed with the SISYFOS package (*39*, *40*). Only one frequency grid was used for the PPLN simulations, because all radiation is polarized along the extraordinary axis of $LiNbO_3$. The grid consisted of 2048 points with 1-PHz width and the central frequency of 500 THz. Because of the spherical symmetry of the propagation, only a quarter of the beam was simulated within a spatial grid of 65 × 65 points and a spacing of about 24 μm in horizontal and vertical directions. In the LGS simulations, three frequency grids of 512 points each were factored out. The grids of seed and pump were centered at 291 THz, whereas the grid of the idler was centered at 100 THz. The bandwidth of each grid was 200 THz. Because of mirror symmetry, only half of the beam profile was simulated for type I phase matching, whereas the full plane was simulated for type II phase matching. The spatial grids had sizes of 128 × 65 and 128 × 128 points, respectively, with a spacing of 1/7 of the pump beam waist in horizontal and vertical directions. The simulations included the materials' dispersion (*29*, *41*), transmission, effective $\chi^{(2)}$-nonlinearities, and (estimated) nonlinear refractive indices. The pump pulses were assumed to be 230 fs long and $sech^2$ shaped, and the seed pulses were retrieved from second-harmonic (LGS OPA) or X-FROG (PPLN OPA) measurements. All beam shapes were assumed to be Gaussian.

SUPPLEMENTARY MATERIALS

Supplementary material for this article is available at http://advances.sciencemag.org/cgi/content/full/4/4/eaaq1526/DC1

section S1. Seed generation in highly nonlinear all-normal dispersion fiber
section S2. Beam distortions in the PPLN OPA
section S3. Compression of the MIR pulses centered at 4.1 μm
section S4. Supercontinuum generation
section S5. LGS OPA
fig. S1. OPA setup with FROG.
fig. S2. All-normal dispersion fiber noise.
fig. S3. Irradiance enhancement in the PPLN OPA.
fig. S4. X-FROG measurements.
fig. S5. Simulation of continuum generation in ZGP.
fig. S6. Properties of the supercontinuum generated by cascaded quadratic nonlinearities in ZGP.
fig. S7. Linear optical properties of LGS.
fig. S8. LGS OPA simulations.
fig. S9. Occurrence of LGS crystal damage at various input powers.
References (*42*–*62*)

REFERENCES AND NOTES

1. P. Hannaford, *Femtosecond Laser Spectroscopy* (Springer-Verlag, ed. 1, 2005).
2. T. Brabec, F. Krausz, Intense few-cycle laser fields: Frontiers of nonlinear optics. *Rev. Mod. Phys.* **72**, 545–591 (2000).
3. F. Krausz, M. I. Stockman, Attosecond metrology: From electron capture to future signal processing. *Nat. Photonics* **8**, 205–213 (2014).
4. S. A. Diddams, The evolving optical frequency comb. *J. Opt. Soc. Am. B* **27**, B51–B62 (2010).
5. M. Müller, M. Kienel, A. Klenke, T. Gottschall, E. Shestaev, M. Plötner, J. Limpert, A. Tünnermann, 1 kW 1 mJ eight-channel ultrafast fiber laser. *Opt. Lett.* **41**, 3439–3442 (2016).
6. S. Antipov, D. D. Hudson, A. Fuerbach, S. D. Jackson, High-power mid-infrared femtosecond fiber laser in the water vapor transmission window. *Optica* **3**, 1373–1376 (2016).
7. V. Petrov, Parametric down-conversion devices: The coverage of the mid-infrared spectral range by solid-state laser sources. *Opt. Mater.* **34**, 536–554 (2012).
8. V. Petrov, Frequency down-conversion of solid-state laser sources to the mid-infrared spectral range using non-oxide nonlinear crystals. *Prog. Quant. Electron.* **42**, 1–106 (2015).
9. T. Südmeyer, E. Innerhofer, F. Brunner, R. Paschotta, T. Usami, H. Ito, S. Kurimura, K. Kitamura, D. C. Hanna, U. Keller, High-power femtosecond fiber-feedback optical parametric oscillator based on periodically poled stoichiometric $LiTaO_3$. *Opt. Lett.* **29**, 1111–1113 (2004).
10. F. Mörz, T. Steinle, A. Steinmann, H. Giessen, Multi-Watt femtosecond optical parametric master oscillator power amplifier at 43 MHz. *Opt. Express* **23**, 23960–23967 (2015).
11. T. Steinle, F. Mörz, A. Steinmann, H. Giessen, Ultra-stable high average power femtosecond laser system tunable from 1.33 to 20 μm. *Opt. Lett.* **41**, 4863–4866 (2016).
12. F. Adler, K. C. Cossel, M. J. Thorpe, I. Hartl, M. E. Fermann, J. Ye, Phase-stabilized, 1.5 W frequency comb at 2.8–4.8 μm. *Opt. Lett.* **34**, 1330–1332 (2009).
13. I. Pupeza, D. Sanchez, J. Zhang, N. Lilienfein, M. Seidel, N. Karpowicz, T. Paasch-Colberg, I. Znakovskaya, M. Pescher, W. Schweinberger, V. Pervak, E. Fill, O. Pronin, Z. Wei, F. Krausz, A. Apolonski, J. Biegert, High-power sub-two-cycle mid-infrared pulses at 100 MHz repetition rate. *Nat. Photonics* **9**, 721–724 (2015).
14. A. Schliesser, N. Picqué, T. W. Hänsch, Mid-infrared frequency combs. *Nat. Photonics* **6**, 440–449 (2012).

15. S. C. Kumar, J. Krauth, A. Steinmann, K. T. Zawilski, P. G. Schunemann, H. Giessen, M. Ebrahim-Zadeh, High-power femtosecond mid-infrared optical parametric oscillator at 7 μm based on $CdSiP_2$. *Opt. Lett.* **40**, 1398–1401 (2015).
16. J. Haas, B. Mizaikoff, Advances in mid-infrared spectroscopy for chemical analysis. *Annu. Rev. Anal. Chem.* **9**, 45–68 (2016).
17. K. C. Cossel, E. M. Waxman, I. A. Finneran, G. A. Blake, J. Ye, N. R. Newbury, Gas-phase broadband spectroscopy using active sources: Progress, status, and applications. *J. Opt. Soc. Am. B* **34**, 104–129 (2017).
18. M. J. Baker, J. Trevisan, P. Bassan, R. Bhargava, H. J. Butler, K. M. Dorling, P. R. Fielden, S. W. Fogarty, N. J. Fullwood, K. A. Heys, C. Hughes, P. Lasch, P. L. Martin-Hirsch, B. Obinaju, G. D. Sockalingum, J. Sulé-Suso, R. J. Strong, M. J. Walsh, B. R. Wood, P. Gardner, F. L. Martin, Using Fourier transform IR spectroscopy to analyze biological materials. *Nat. Protoc.* **9**, 1771–1791 (2014).
19. E. J. Heilweil, Ultrashort-pulse multichannel infrared spectroscopy using broadband frequency conversion in $LiIO_3$. *Opt. Lett.* **14**, 551–553 (1989).
20. P. Hamm, M. Zanni, *Concepts and Methods of 2D Infrared Spectroscopy* (Cambridge Univ. Press, 2011).
21. T. Popmintchev, M.-C. Chen, D. Popmintchev, P. Arpin, S. Brown, S. Ališauskas, G. Andriukaitis, T. Balčiunas, O. D. Mücke, A. Pugzlys, A. Baltuška, B. Shim, S. E. Schrauth, A. Gaeta, C. Hernández-García, L. Plaja, A. Becker, A. Jaron-Becker, M. M. Murnane, H. C. Kapteyn, Bright coherent ultrahigh harmonics in the keV X-ray regime from mid-infrared femtosecond lasers. *Science* **336**, 1287–1291 (2012).
22. O. Schubert, M. Hohenleutner, F. Langer, B. Urbanek, C. Lange, U. Huttner, D. Golde, T. Meier, M. Kira, S. W. Koch, R. Huber, Sub-cycle control of terahertz high-harmonic generation by dynamical Bloch oscillations. *Nat. Photonics* **8**, 119–123 (2014).
23. A. Rogalski, History of infrared detectors. *Opto-Electron. Rev.* **20**, 279–308 (2012).
24. L. Maidment, Z. Zhang, C. R. Howle, D. T. Reid, Stand-off identification of aerosols using mid-infrared backscattering Fourier-transform spectroscopy. *Opt. Lett.* **41**, 2266–2269 (2016).
25. O. Pronin, J. Brons, C. Grasse, V. Pervak, G. Boehm, M.-C. Amann, V. L. Kalashnikov, A. Apolonski, F. Krausz, High-power 200 fs Kerr-lens mode-locked Yb:YAG thin-disk oscillator. *Opt. Lett.* **36**, 4746–4748 (2011).
26. N. Thiré, R. Maksimenka, B. Kiss, C. Ferchaud, P. Bizouard, E. Cormier, K. Osvay, N. Forget, 4-W, 100-kHz, few-cycle mid-infrared source with sub-100-mrad carrier-envelope phase noise. *Opt. Express* **25**, 1505–1514 (2017).
27. Data extracted from SNLO software (V. 66); http://www.as-photonics.com/snlo.
28. B. Luther-Davies, Y. Yu, Efficient generation of ultra-short pulses in the infrared from a simple PPLN optical parametric amplifier, in *Nonlinear Optics* (Optical Society of America, 2017), p. NTu2A.4.
29. L. Isaenko, A. Yelisseyev, S. Lobanov, A. Titov, V. Petrov, J.-J. Zondy, P. Krinitsin, A. Merkulov, V. Vedenyapin, J. Smirnova, Growth and properties of $LiGaX_2$ (X = S, Se, Te) single crystals for nonlinear optical applications in the mid-IR. *Cryst. Res. Technol.* **38**, 379–387 (2003).
30. P. G. Schunemann, K. T. Zawilski, L. A. Pomeranz, D. J. Creeden, P. A. Budni, Advances in nonlinear optical crystals for mid-infrared coherent sources. *J. Opt. Soc. Am. B* **33**, D36–D43 (2016).
31. E. E. Hoover, J. A. Squier, Advances in multiphoton microscopy technology. *Nat. Photonics* **7**, 93–101 (2013).
32. C. R. Petersen, U. Møller, I. Kubat, B. Zhou, S. Dupont, J. Ramsay, T. Benson, S. Sujecki, N. Abdel-Moneim, Z. Tang, D. Furniss, A. Seddon, O. Bang, Mid-IR supercontinuum covering the 1.4–13.3 μm molecular fingerprint region using ultra-high NA chalcogenide step-index fibre. *Nat. Photonics* **8**, 830–834 (2014).
33. A. A. Lanin, A. A. Voronin, E. A. Stepanov, A. B. Fedotov, A. M. Zheltikov, Multioctave, 3-18 μm sub-two-cycle supercontinua from self-compressing, self-focusing soliton transients in a solid. *Opt. Lett.* **40**, 974–977 (2015).
34. M. Seidel, J. Brons, G. Arisholm, K. Fritsch, V. Pervak, O. Pronin, Efficient high-power ultrashort pulse compression in self-defocusing bulk media. *Sci. Rep.* **7**, 1410 (2017).
35. H. Liang, P. Krogen, Z. Wang, H. Park, T. Kroh, K. Zawilski, P. Schunemann, J. Moses, L. F. DiMauro, F. X. Kärtner, K.-H. Hong, High-energy mid-infrared sub-cycle pulse synthesis from a parametric amplifier. *Nat. Commun.* **8**, 141 (2017).
36. L. M. Miller, M. J. Tobin, S. Chio-Srichan, P. Dumas, The use of synchrotron radiation for biomedical applications of infrared microscopy, in *Biological and Biomedical Infrared Spectroscopy*, A. Barth, P. I. Haris, Eds. (IOS Press, 2009).
37. R. A. Ganeev, I. A. Kulagin, A. I. Ryasnyanskii, R. I. Tugushev, T. Usmanov, The nonlinear refractive indices and nonlinear third-order susceptibilities of quadratic crystals. *Opt. Spectrosc.* **94**, 561–568 (2003).
38. Y. Liu, Y. Zhao, J. Lyngsø, S. You, W. L. Wilson, H. Tu, S. A. Boppart, Suppressing short-term polarization noise and related spectral decoherence in all-normal dispersion fiber supercontinuum generation. *J. Lightwave Technol.* **33**, 1814–1820 (2015).
39. G. Arisholm, General numerical methods for simulating second-order nonlinear interactions in birefringent media. *J. Opt. Soc. Am. B* **14**, 2543–2549 (1997).
40. G. Arisholm, H. Fonnum, Simulation System For Optical Science (SISYFOS)—tutorial (2012); http://www.ffi.no/no/Rapporter/12-02042.pdf [accessed 9 March 2018].
41. O. Gayer, Z. Sacks, E. Galun, A. Arie, Temperature and wavelength dependent refractive index equations for MgO-doped congruent and stoichiometric $LiNbO_3$. *Appl. Phys. B* **91**, 343–348 (2008).
42. J. M. Dudley, G. Genty, S. Coen, Supercontinuum generation in photonic crystal fiber. *Rev. Mod. Phys.* **78**, 1135–1184 (2006).
43. A. M. Heidt, Pulse preserving flat-top supercontinuum generation in all-normal dispersion photonic crystal fibers. *J. Opt. Soc. Am. B* **27**, 550–559 (2010).
44. T. Steinle, A. Steinmann, R. Hegenbarth, H. Giessen, Watt-level optical parametric amplifier at 42 MHz tunable from 1.35 to 4.5 μm coherently seeded with solitons. *Opt. Express* **22**, 9567–9573 (2014).
45. M. Baudisch, M. Hemmer, H. Pires, J. Biegert, Performance of MgO:PPLN, KTA, and $KNbO_3$ for mid-wave infrared broadband parametric amplification at high average power. *Opt. Lett.* **39**, 5802–5805 (2014).
46. P. Rigaud, A. Van de Walle, M. Hanna, N. Forget, F. Guichard, Y. Zaouter, K. Guesmi, F. Druon, P. Georges, Supercontinuum-seeded few-cycle mid-infrared OPCPA system. *Opt. Express* **24**, 26494–26502 (2016).
47. M. Seidel, G. Arisholm, J. Brons, V. Pervak, O. Pronin, All solid-state spectral broadening: An average and peak power scalable method for compression of ultrashort pulses. *Opt. Express* **24**, 9412–9428 (2016).
48. M. Sheik-Bahae, D. J. Hagan, E. W. Van Stryland, Dispersion and band-gap scaling of the electronic Kerr effect in solids associated with two-photon absorption. *Phys. Rev. Lett.* **65**, 96–99 (1990).
49. D. E. Zelmon, E. A. Hanning, P. G. Schunemann, Refractive-index measurements and Sellmeier coefficients for zinc germanium phosphide from 2 to 9 μm with implications for phase matching in optical frequency-conversion devices. *J. Opt. Soc. Am. B* **18**, 1307–1310 (2001).
50. Z. Zhao, X. Wang, S. Dai, Z. Pan, S. Liu, L. Sun, P. Zhang, Z. Liu, Q. Nie, X. Shen, R. Wang, 1.5-14 μm midinfrared supercontinuum generation in a low-loss Te-based chalcogenide step-index fiber. *Opt. Lett.* **41**, 5222–5225 (2016).
51. U. Møller, Y. Yu, I. Kubat, C. R. Petersen, X. Gai, L. Brilland, D. Méchin, C. Caillaud, J. Troles, B. Luther-Davies, O. Bang, Multi-milliwatt mid-infrared supercontinuum generation in a suspended core chalcogenide fiber. *Opt. Express* **23**, 3282–3291 (2015).
52. S. Kedenburg, T. Steinle, F. Mörz, A. Steinmann, H. Giessen, High-power mid-infrared high repetition-rate supercontinuum source based on a chalcogenide step-index fiber. *Opt. Lett.* **40**, 2668–2671 (2015).
53. R. DeSalvo, D. J. Hagan, M. Sheik-Bahae, G. Stegeman, E. W. Van Stryland, H. Vanherzeele, Self-focusing and self-defocusing by cascaded second-order effects in KTP. *Opt. Lett.* **17**, 28–30 (1992).
54. J. Moses, F. W. Wise, Controllable self-steepening of ultrashort pulses in quadratic nonlinear media. *Phys. Rev. Lett.* **97**, 073903 (2006).
55. M. Bache, H. Guo, B. Zhou, Generating mid-IR octave-spanning supercontinua and few-cycle pulses with solitons in phase-mismatched quadratic nonlinear crystals. *Opt. Mater. Express* **3**, 1647–1657 (2013).
56. B. Zhou, M. Bache, Invited Article: Multiple-octave spanning high-energy mid-IR supercontinuum generation in bulk quadratic nonlinear crystals. *APL Photonics* **1**, 050802 (2016).
57. T. Kanai, P. Malevich, S. S. Kangaparambil, K. Ishida, M. Mizui, K. Yamanouchi, H. Hoogland, R. Holzwarth, A. Pugzlys, A. Baltuska, Parametric amplification of 100 fs mid-infrared pulses in $ZnGeP_2$ driven by a Ho:YAG chirped-pulse amplifier. *Opt. Lett.* **42**, 683–686 (2017).
58. A. Couairon, A. Mysyrowicz, Femtosecond filamentation in transparent media. *Phys. Rep.* **441**, 47–189 (2007).
59. A. Hache, J. E. Sipe, H. M. van Driel, Quantum interference control of electrical currents in GaAs. *IEEE J. Quant. Electron.* **34**, 1144–1154 (1998).
60. V. Petrov, A. Yelisseyev, L. Isaenko, S. Lobanov, A. Titov, J.-J. Zondy, Second harmonic generation and optical parametric amplification in the mid-IR with orthorhombic biaxial crystals $LiGaS_2$ and $LiGaSe_2$. *Appl. Phys. B* **78**, 543–546 (2004).
61. A. Tyazhev, V. Vedenyapin, G. Marchev, L. Isaenko, D. Kolker, S. Lobanov, V. Petrov, A. Yelisseyev, M. Starikova, J.-J. Zondy, Singly-resonant optical parametric oscillation based on the wide band-gap mid-IR nonlinear optical crystal $LiGaS_2$. *Opt. Mater.* **35**, 1612–1615 (2013).
62. K. Kaneshima, N. Ishii, K. Takeuchi, J. Itatani, Generation of carrier-envelope phase-stable mid-infrared pulses via dual-wavelength optical parametric amplification. *Opt. Express* **24**, 8660–8665 (2016).

Acknowledgments: We thank W. Schweinberger, I. Pupeza, and N. Karpowicz for helpful discussions. **Funding:** Financial support was provided by the Munich-Centre for Advanced Photonics, grant EXC 158 of the Deutsche Forschungsgemeinschaft. **Author contributions:** M.S. conceived and conducted the experiments and performed the simulations. X.X. set up the

PPLN OPA. S.A.H. supported the PPLN OPA noise measurements. G.A. developed and adapted the simulation package. A.H. advised on fiber selection and prepared fibers. K.T.Z. and P.G.S. manufactured the supercontinuum-generating ZGP crystal. F.H., M.T., and V.P. designed, coated, and characterized the NIR/MIR beam splitters. O.P. and F.K. supervised and guided the project. M.S., X.X., S.A.H., G.A., A.H., P.G.S., O.P., and F.K. discussed the manuscript. **Competing interests:** The authors declare that they have no competing interests. **Data and materials availability:** All data needed to evaluate the conclusions in the paper are present in the paper and/or the Supplementary Materials. Additional data related to this paper may be requested from the authors.

Submitted 3 November 2017
Accepted 13 March 2018
Published 20 April 2018
10.1126/sciadv.aaq1526

Citation: M. Seidel, X. Xiao, S. A. Hussain, G. Arisholm, A. Hartung, K. T. Zawilski, P. G. Schunemann, F. Habel, M. Trubetskov, V. Pervak, O. Pronin, F. Krausz, Multi-watt, multi-octave, mid-infrared femtosecond source. *Sci. Adv.* **4**, eaaq1526 (2018).

Science Advances

Multi-watt, multi-octave, mid-infrared femtosecond source

Marcus Seidel, Xiao Xiao, Syed A. Hussain, Gunnar Arisholm, Alexander Hartung, Kevin T. Zawilski, Peter G. Schunemann, Florian Habel, Michael Trubetskov, Vladimir Pervak, Oleg Pronin and Ferenc Krausz

Sci Adv **4** (4), eaaq1526.
DOI: 10.1126/sciadv.aaq1526

Science Advances (ISSN 2375-2548) is published by the American Association for the Advancement of Science, 1200 New York Avenue NW, Washington, DC 20005. The title *Science Advances* is a registered trademark of AAAS.